Structure

Article

Structural characterization of Thogoto Virus nucleoprotein provides insights into viral RNA encapsidation and RNP assembly

Graphical abstract

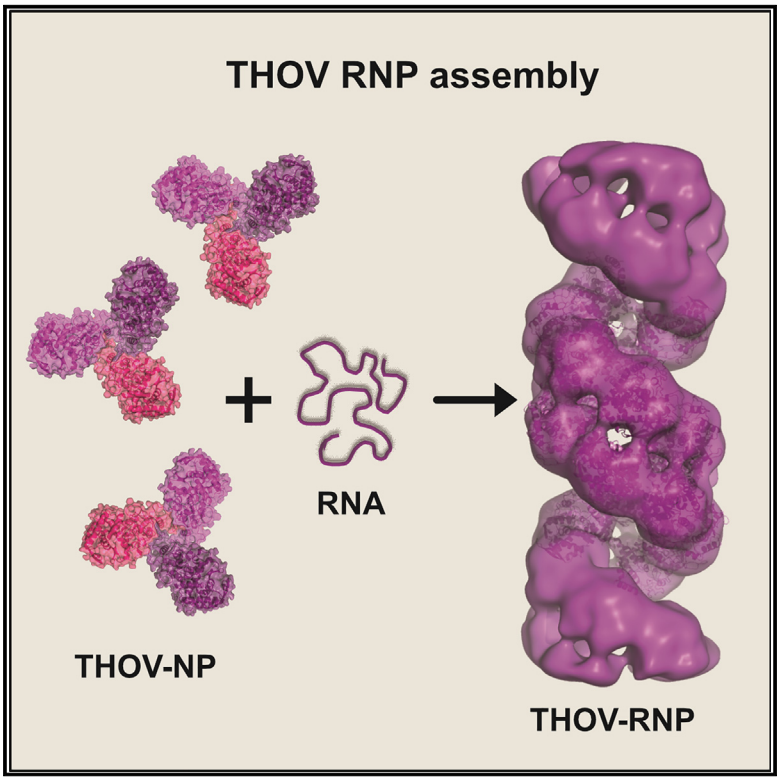

Authors

Alexej Dick, Vasilii Mikirtumov, Jonas Fuchs, ..., Georg Kochs, Yvette Roske, Oliver Daumke

Correspondence

georg.kochs@uniklinik-freiburg.de (G.K.), yroske@mdc-berlin.de (Y.R.), oliver.daumke@mdc-berlin.de (O.D.)

In brief

Dick et al. determined structures of the trimeric orthomyxovirus Thogoto virus nucleoprotein and the native ribonucleoprotein complex. They identified and functionally characterized the RNA-binding groove and the oligomerization mode. Their study elucidates promising sites for the development of antivirals drugs, which interfere with RNA binding or oligomerization.

Highlights

- The trimeric THOV NP crystal structure was determined
- RNA-binding groove of THOV NP was identified
- THOV NP tail loop mutations interfere with oligomerization and viral replication
- A cryo-ET reconstruction of THOV RNP revealed a left-handed helical architecture

Dick et al., 2024, Structure *32*, 1–11
August 8, 2024
https://doi.org/10.1016/j.str.2024.04.016

CellPress

Structure

CellPress
OPEN ACCESS

Article

Structural characterization of Thogoto Virus nucleoprotein provides insights into viral RNA encapsidation and RNP assembly

Alexej Dick,[1,2,6] Vasilii Mikirtumov,[1,2] Jonas Fuchs,[3] Ferdinand Krupp,[1] Daniel Olal,[1] Elias Bendl,[3] Thiemo Sprink,[1,4] Christoph Diebolder,[4] Mikhail Kudryashev,[1,5] Georg Kochs,[3,*] Yvette Roske,[1,*] and Oliver Daumke[1,2,7,*]

[1]From Structural Biology, Max-Delbrück Center for Molecular Medicine in the Helmholtz Association, Robert-Rössle-Straße 10, 13125 Berlin, Germany
[2]Institute of Chemistry and Biochemistry, Freie Universität Berlin, Takustraße 6, 14195 Berlin, Germany
[3]Institute of Virology, Medical Center - University of Freiburg, Faculty of Medicine, University of Freiburg, Hermann-Herder-Straße 11, 79104 Freiburg, Germany
[4]Core facility for Cryo-Electron Microscopy, Charité, Berlin, Germany
[5]Institute of Medical Physics and Biophysics, Charité-Universitätsmedizin Berlin, Berlin, Germany
[6]Present address: Department of Biochemistry and Molecular Biology, Drexel University College of Medicine, 245 North 15th Street, New College Building, Philadelphia, Pennsylvania, 19102, USA
[7]Lead contact
*Correspondence: georg.kochs@uniklinik-freiburg.de (G.K.), yroske@mdc-berlin.de (Y.R.), oliver.daumke@mdc-berlin.de (O.D.)
https://doi.org/10.1016/j.str.2024.04.016

SUMMARY

Orthomyxoviruses, such as influenza and thogotoviruses, are important human and animal pathogens. Their segmented viral RNA genomes are wrapped by viral nucleoproteins (NPs) into helical ribonucleoprotein complexes (RNPs). NP structures of several influenza viruses have been reported. However, there are still contradictory models of how orthomyxovirus RNPs are assembled. Here, we characterize the crystal structure of Thogoto virus (THOV) NP and found striking similarities to structures of influenza viral NPs, including a two-lobed domain architecture, a positively charged RNA-binding cleft, and a tail loop important for trimerization and viral transcription. A low-resolution cryo-electron tomography reconstruction of THOV RNPs elucidates a left-handed double helical assembly. By providing a model for RNP assembly of THOV, our study suggests conserved NP assembly and RNA encapsidation modes for thogoto- and influenza viruses.

INTRODUCTION

Orthomyxoviruses comprise a family of enveloped viruses with a segmented, negative-sense, single-stranded (ss) RNA genome that includes influenza viruses, thogotoviruses, Quaranja virus, and the monotypic genera Isa virus, Mykiss virus, and Sardino virus.[1–3] Their segmented genome provides them with high genomic flexibility that can facilitate adaptation to new host species. While influenza viruses have garnered high attention,[4] less is known about the related thogotoviruses that are transmitted by ticks. As of 2023, the genus thogotovirus consists of eight recognized species, of which the eponymous Thogoto virus (THOV), Dhori virus (DHOV), and, more recently, Bourbon virus (BRBV) and Oz virus (OZV) have been shown to sporadically infect humans, causing a febrile disease with occasional fatal outcome.[5–7] In sheep, THOV infection causes febrile illness and abortions.[8] In experimentally infected mice, THOV and DHOV lead to a fatal disease accompanied by lesions of the liver and lung.[9–11]

THOV has a ssRNA genome of ~10 kb, which is organized into six segments. Each segment encodes a structural protein, such as the envelope glycoprotein that confers attachment to host cells, the matrix protein that mediates assembly and budding, the heterotrimeric viral RNA-dependent RNA polymerase (RdRP) composed of subunits PA, PB1, and PB2 and the nucleoprotein (NP) that decorates the viral RNA. Genomic and structural analyses of THOV polypeptides support an evolutionary link to influenza viruses. Accordingly, the viral polymerase subunits of THOV and influenza A virus (IAV) have related folds.[12]

A hallmark of negative-sense viral RNA genomes is their association with multiple copies of the viral NP. Together with the viral RdRP, the NP and the viral RNA constitute the viral ribonucleoprotein complexes (RNPs) (reviewed by Eisfeld A.J.[13]). Viral NPs are multifunctional proteins. They encapsidate RNA into RNPs, which are transcription- and replication-competent; they protect the viral genome from degradation and prevent double strand (ds) RNA formation. Translocation signals in the NP account for the intracellular transport of the RNPs and interactions with viral or cellular proteins at the plasma membrane promote packaging of the RNPs into infectious progeny virions.[14]

RNA-bound NP structures of vesicular stomatitis and rabies virus provided the first insights into how ssRNA binds to the NP at the interface of two prominent lobes.[15,16] Likewise, the

Please cite this article in press as: Dick et al., Structural characterization of Thogoto Virus nucleoprotein provides insights into viral RNA encapsidation and RNP assembly, Structure (2024), https://doi.org/10.1016/j.str.2024.04.016

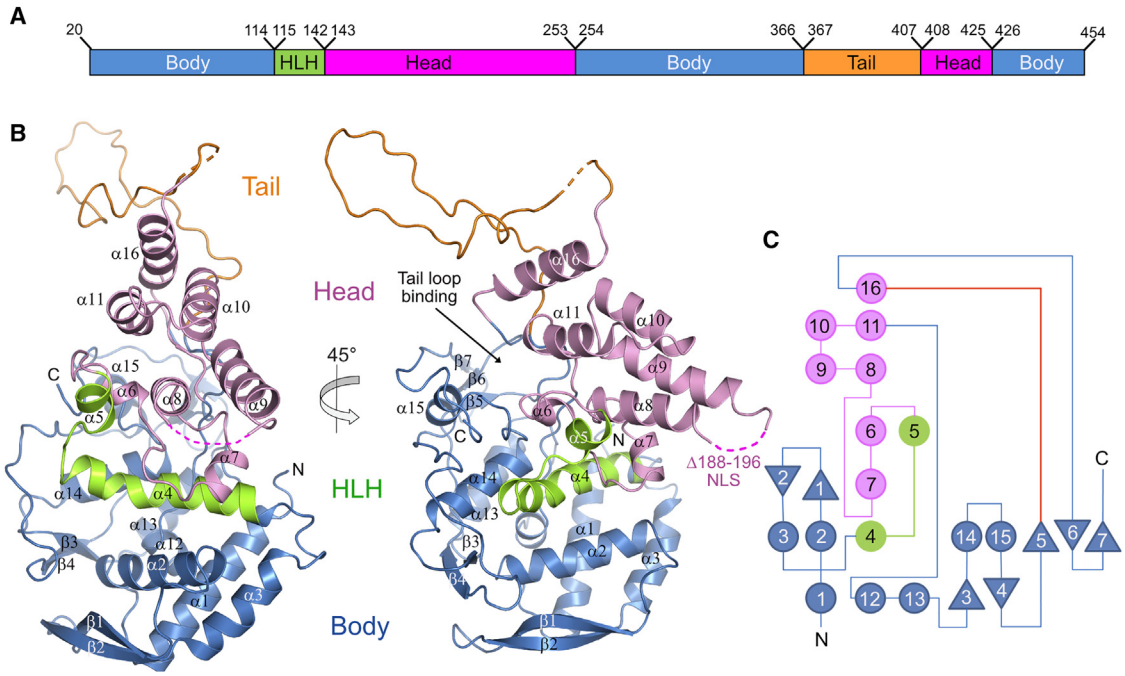

Figure 1. Structure and domain architecture of the THOV NP$^{\Delta 188\text{-}196}$

(A) Schematic representation of the domain architecture of THOV NP$^{\Delta 188\text{-}196}$. Unresolved residues are 1–19, 184–196, 402–403.

(B) Two-sided cartoon representations of the THOV NP$^{\Delta 188\text{-}196}$ structure. The first visible amino acid is Thr20. The body and head domain, helix-loop helix motive, and tail loop are colored in blue, pink, green, and orange, respectively.

(C) Topology diagram of the THOV NP structure with α-helices in circle- and β strands in triangle representation, with the same color code as in B. See also Figures S1 and S2, Tables S1 and S2.

NPs of Arena-, Bunya-, and Hantaviruses have a two-lobed architecture, with N- and C-terminal extensions mediating oligomerization.[17] NP structures of IAV,[18,19] influenza B virus (IBV),[18] influenza D virus (IDV)[20] and infectious salmon anemia virus (ISAV)[21] show a related NP fold with a mainly α-helical structure, containing a positively charged RNA-binding groove between the upper and lower lobes. In the crystal structures, their tail loops mediate oligomerization by binding into a cleft of an adjacent NP molecule.

Native and recombinant RNPs of IAV were visualized using cryo-electron microscopy (cryo-EM).[22–24] Interestingly, the two reported RNP models were strikingly different in their architecture: Whereas Moeller et al. suggested a right-handed double-helical model with two antiparallel strands, Arranz et al. described a left-handed helical arrangement displaying a double-helical arrangement in which two NP strands of opposite polarity are associated with each other along the helix. Within the RNPs, the complementary end sequences of the ssRNA strands are connected and form a pan-handle structure that is bound by the viral RdRp. During transcription, the flexibility of the viral RNPs may permit the polymerase complex to perform a sliding movement between the antiparallel NP-RNA strands while still interacting with both RNA ends.[23]

To understand the structural details of the THOV RNP assemblies and their biological function, we determined its NP crystal structure in the current work. Similar to IAV NP, we identify an RNA-binding site in a groove of THOV NP between the upper and lower lobe and a tail loop that deeply inserts into a pocket of the neighboring molecule within an NP trimer. Accordingly, mutations in the tail loop interfered with oligomerization and viral replication. A cryo-electron tomography (cryo-ET) reconstruction of native THOV RNPs revealed a left-handed helical architecture similar to that described by Arranz and colleagues for the IAV RNPs.[22] Our structural work suggests a related assembly and RNA encapsidation modes for THOV NP and those of other orthomyxoviruses.

RESULTS

Crystal structure of THOV NP

To obtain structural information of full-length THOV NP, the protein was expressed with an N-terminal His_6-tag in bacteria and purified to homogeneity (Figures S1A and S1B). Despite extensive crystallization attempts, only poorly diffracting crystals were obtained. Based on sequence alignments (Table S1) and secondary structure predictions, we identified several flexible loop regions that could interfere with the formation of highly ordered crystals. Deletion of one of these loops (residues 188–196) in the THOV NP$^{\Delta 188\text{-}196}$ construct yielded a soluble protein. This construct crystallized in space group R3, and crystals diffracted X-rays to 2.0 Å resolution (Table S2). The phase problem was solved by single-wavelength anomalous dispersion (SAD) using selenomethionine-substituted crystals, and the structure was refined to an R_{work}/R_{free} of 18.5%/23.4% (Table S2).

The bean-shaped THOV NP structure comprises a head and a body domain (Figures 1A and 1B). It is primarily α-helical, with

Please cite this article in press as: Dick et al., Structural characterization of Thogoto Virus nucleoprotein provides insights into viral RNA encapsidation and RNP assembly, Structure (2024), https://doi.org/10.1016/j.str.2024.04.016

CellPress
OPEN ACCESS

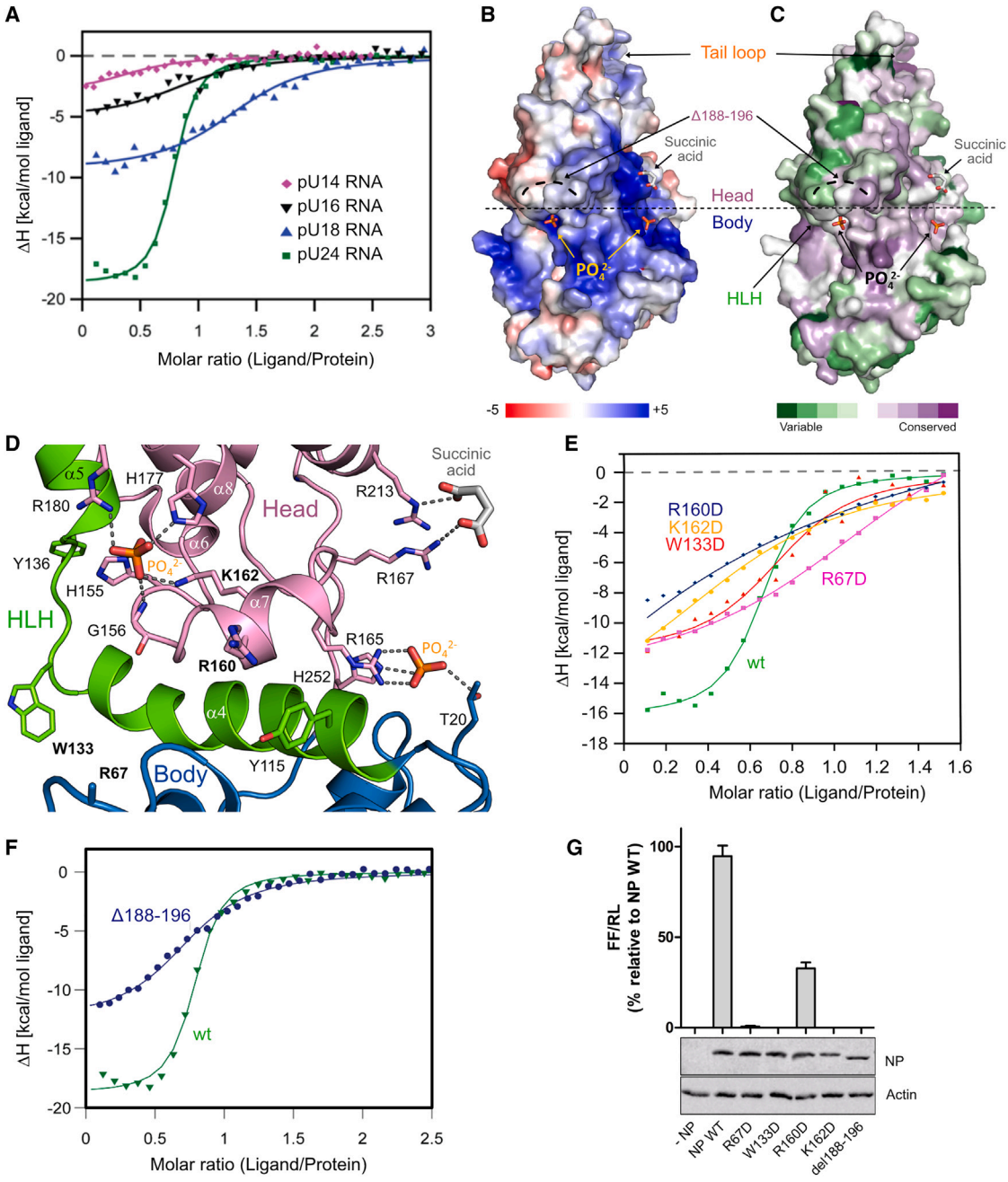

Figure 2. A conserved RNA-binding groove mediates RNA interaction

(A) ITC data of full length THOV NP binding to polyU RNA oligomers of different lengths. Resulting heat changes upon ligand titration in a VP-ITC device were integrated and plotted, and the following K_D values were obtained; pU24: $K_D = 130 \pm 20$ nM, $n = 0.80 \pm 0.01$; pU18: $K_D = 430 \pm 90$ nM, $n = 1.40 \pm 0.03$; pU16: $K_D = 1.2 \pm 0.4$ μM, $n = 0.90 \pm 0.06$ and pU14: $K_D = 2 \pm 1$ μM, $n = 0.50 \pm 0.08$. Reported errors represent standard deviations of the fit.

(B) Electrostatic surface potential map of the THOV NP$^{\Delta 188\text{-}196}$ (view on the positively charged RNA binding groove) with positioned small molecules phosphates, ethylene glycol, and succinic acid. The color range, calculated at 310 K is from −5 kcal/mol*e (red) to +5 kcal/mol*e (blue).

(C) Surface conservation plot of the THOV NP$^{\Delta 188\text{-}196}$ considering the orthomyxovirus sequences displayed in Table S1. Shown is the same orientation as in B. The color range indicates the degree of conservation (purple 100% and green ≥50% conservation).

(D) A detailed view highlights the binding of phosphates and succinate within the RNA-binding groove, indicating possible key residues involved in RNA binding. HLH, Helix-loop-helix motif.

(E) Integrated ITC thermograms for full length THOV NP and mutants in the RNA-binding groove (WT in green, R67D in pink, W133D in red, R160D in blue, and K162D in orange) titrated with pU24mer and fitted to a 1:1 binding model. Values obtained from measurements at iTC200 instrument are displayed in Table S3. Reported errors represent standard deviations of the fit.

(legend continued on next page)

Please cite this article in press as: Dick et al., Structural characterization of Thogoto Virus nucleoprotein provides insights into viral RNA encapsidation and RNP assembly, Structure (2024), https://doi.org/10.1016/j.str.2024.04.016

small β sheets located in the body domain (Figures 1B and 1C; Table S1). A prominent tail loop (residues 367–407) protrudes from the tip of the head. The polypeptide chain moves back and forth between the body and head domain via a helix-loop-helix motif (α4-loop-α5) and an elongated loop region between a11 and a12 (residues 244–256), leading to an interspersed architecture of the two domains (Figure 1). The first N-terminal 19 residues are disordered.

Structural comparisons revealed a remarkable similarity of THOV NP to the NPs of other orthomyxoviruses despite a low sequence conservation of only 10–15% (Figure S2A). The closest structural similarity was observed to the IAV NP, with a root-mean-square deviation (RMSD) of 2.5 Å over 337 Cα-atoms. Moreover, comparisons of THOV NP with those of other negative-sense ssRNA viruses showed overall related topologies despite remarkable differences in size and primary sequence (Figure S2B). In all cases, a head and a body domain are connected via one or two loop regions and a characteristic central helix-loop-helix motif surrounding the RNA-binding groove. Also, in the other NPs, these regions are spread throughout the whole sequence, providing the NPs with stability and the flexibility crucial for encapsidating the viral genome.[25] Together, the structural similarity and conservation indicate a functional conservation of the NP architecture for viral RNA encapsidation and transcription in negative-stranded ssRNA viruses.

Identification of the RNA-binding cleft

To obtain insights into RNA binding to the THOV NP, we tested the interaction with ss poly-uridine (polyU) oligomers of various lengths using isothermal titration calorimetry. PolyU was chosen to avoid formation of secondary structures in the RNA. In these experiments, the THOV NP showed high affinity toward a 24-mer polyU, with a dissociation constant (K_D) of 130 ± 20 nM. Shorter RNA molecules decreased affinity to a K_D of 2 ± 1 μM for the 14-mer polyU (Figure 2A). For all ITC titration experiments, a stoichiometry value of N ∼1 was determined, reflecting a binding ratio of one THOV-NP protomer to one molecule RNA.

In THOV NP, a positively charged groove is situated between the head and body domain (Figure 2B), which is highly conserved between NPs of orthomyxoviruses (Figure 2C). We reasoned that similar to IAV NP,[26] this cleft might constitute the RNA-binding site (Figure S2B). Accordingly, multiple basic residues in THOV NP, such as Arg67, Arg160, Lys162, and Arg165, are located in this region (Figure 2D). Also, aromatic residues, such as Tyr115, Trp133, and Tyr136, could contribute to RNA binding and stabilization by forming π-π-stacking interactions with the RNA bases.[27] Interestingly, anions such as succinic acid and phosphates from the crystallization solution were bound in the putative RNA-binding groove of THOV $NP^{\Delta 188\text{-}196}$. In the absence of RNA, these negatively charged ions can indicate potential RNA-binding sites. One phosphate ion is coordinated by positively charged residues (His155, Lys162, His177, and Arg180) and the carbon-nitrogen of Gly156 (Figure 2D). The second phosphate ion is stabilized by Thr20, Arg165, and His252 (Figure 2D). Adjacent to the second phosphate ion, a succinic acid molecule contacts Arg167 and Arg213 (Figure 2D). These sites form a belt-like, elongated 36 Å long, transverse structure between body and head domain that may accommodate the viral RNA.

To analyze the function of this groove for RNA binding, central residues within the groove were mutated (Figure 2E; Table S3). The W133D mutation reduced binding affinity to the 24-mer polyU 3-fold, the R67D 10-fold, and the K162D mutation 15-fold. No saturation was reached with the R160D mutant. Removal of residues 188–196, as in the crystallization construct, reduced affinity for the polyU 24-mer by a factor of nine, suggesting a pivotal contribution of this loop to RNA binding (Figure 2F). We also tested how these RNA-binding mutants affect viral transcription, using a THOV polymerase reconstitution assay. All mutations completely abolished transcriptional activity except for R160D, which led to reduced transcriptional activity (Figure 2G). These results align with the groove's proposed role in RNA binding and directly link the RNA binding capacity of NP to viral transcriptional activity.

Trimerization of THOV NP

In right-angle light scattering (RALS) experiments, THOV NP displayed a trimeric assembly state at physiological salt concentrations (Figure 3A). Also in analytical ultracentrifugation (AUC), THOV NP yielded a sedimentation coefficient for a trimer (Figure S1C). Accordingly, a trimer was also observed in the crystals of THOV $NP^{\Delta 188\text{-}196}$ via a 3-fold crystallographic axis (Figure 3B). The interaction was mediated by the positively charged tail loop that protruded into a negatively charged and partially hydrophobic elongated pocket located between the head and the body domain of the neighboring NP (Figures 3C and 3D). Helix α16 interacts with both adjacent protomers in the trimeric interface (Figures 3B and 3D).

The tip of the tail loop is stabilized by an extensive hydrogen bond network and salt bridges formed by Arg386-Glu316 and Asn391-Asn449 (Figure 3D). Additionally, Arg386 forms intra-tail loop stabilizing contacts to the carbonyl oxygens of Phe382 and Gly384. The prominent and conserved Phe382 stacks with the hydrophobic clusters Phe253, Phe277, Phe311, and Phe431 at the pocket's base (Figure 3D).

In line with our crystallographic data, truncation of the tail loop (e.g., amino acids 378–387) or mutations (F382D and R386A) interfered with THOV NP trimerization (Figure 3E). In contrast, the E316A exchange in the pocket did not completely abolish trimerization of THOV NP (Figure 3E), unlike the related exchanges in IAV and IBV NPs.[19,28] Interestingly, the monomeric R386A tail loop mutant showed an 11-fold reduced binding to the 24-mer polyU RNA compared to wild type (WT) (Figure 3F; Table S3), indicating that trimerization or higher-order

(F) ITC experiments performed with an VP-ITC, showing binding of the THOV $NP^{\Delta 188\text{-}196}$ construct (blue) to pU24 with K_D = 1.1 ± 0.1 μM, n = 0.80 ± 0.02 versus WT THOV NP (green) with K_D = 130 ± 20 nM, n = 0.80 ± 0.01. Reported errors represent standard deviations of the fit.
(G) THOV polymerase activity in a reconstitution assay using WT THOV NP and the indicated mutants. Expression of the transfected cDNA constructs encoding NP was monitored by western blot analysis. Detection of actin was used as a loading control. Shown are mean ± SD of three independent experiments. See also Table S3.

Please cite this article in press as: Dick et al., Structural characterization of Thogoto Virus nucleoprotein provides insights into viral RNA encapsidation and RNP assembly, Structure (2024), https://doi.org/10.1016/j.str.2024.04.016

CellPress
OPEN ACCESS

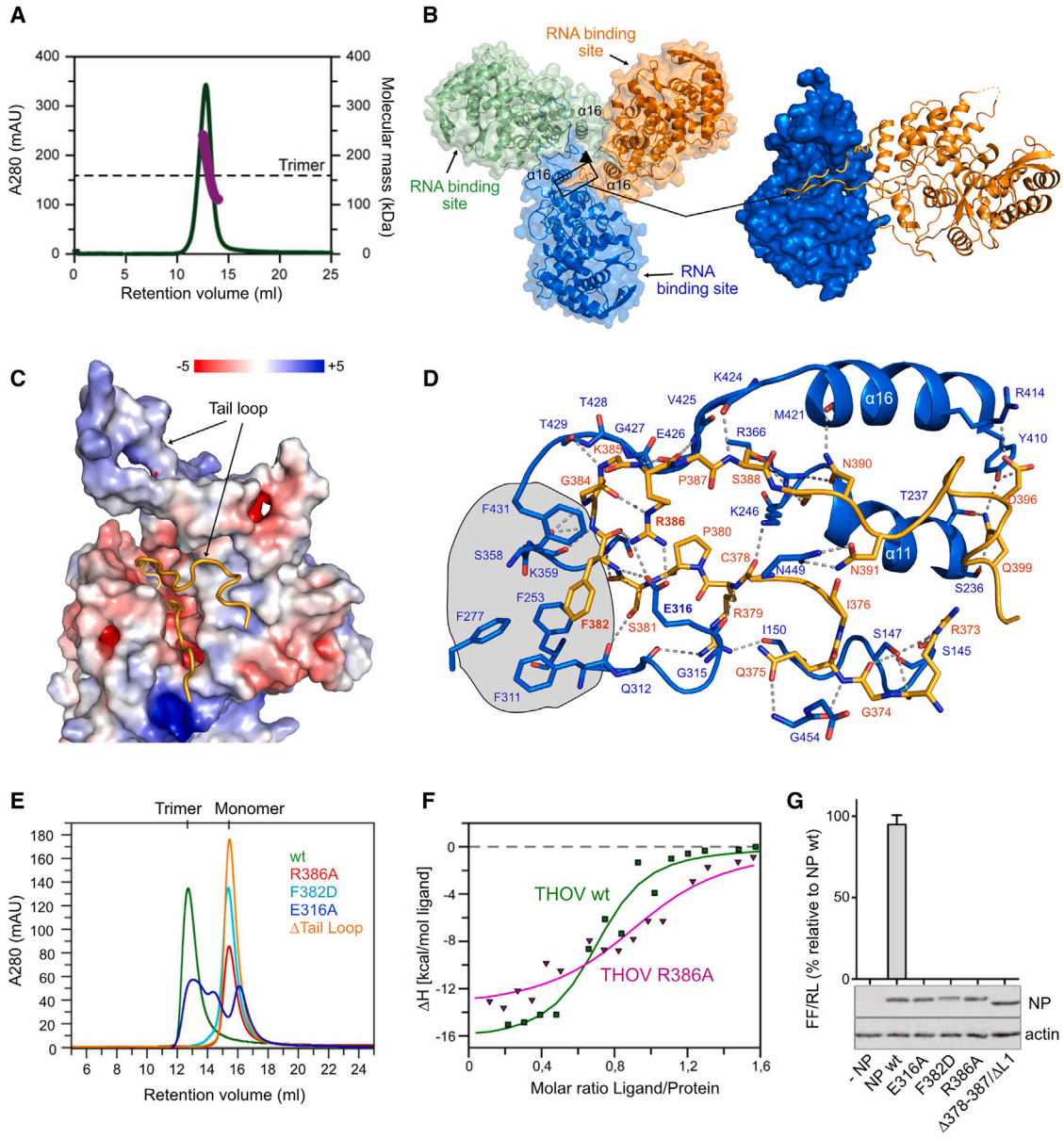

Figure 3. THOV NP trimerization

(A) Full-length THOV NP applied on an analytical S200 10/300 gel filtration column connected to a RALS detector. The purple curve refers to the RALS signal (right y axis) and indicates the average molecular mass within the eluted peak.

(B) Within the crystal, THOV NP$^{\Delta 188\text{-}196}$ assembles via a 3-fold axis (triangle) into a homotrimer. The protomers are shown in blue, green, and orange cartoon structures with transparent surfaces. The tail loop insertion of one protomer (shown as orange cartoon) into the deep, elongated binding pocket of the adjacent THOV NP protomer (shown as blue surface) is shown at the right.

(C) Electrostatic surface potential map of one THOV NP protomer depicts the negatively charged tail loop binding groove and the positively charged tail loop. Color, calculated at 310 K, is from −5 kcal/mol*e (red) to +5 kcal/mol*e (blue). The neighboring protomer's tail loop insertion is shown as an orange line.

(D) Detailed interaction within the interprotomer interface with polar contacts shown as dashed lines and hydrophobic region highlighted in light gray. Tail loop (residues 373–400) in orange, residues forming the pocket in blue.

(E) Preparative gel filtration of full-length THOV NP WT, tail loop mutants, and a variant containing a partial deletion of the tail loop (residues 378–387).

(F) Monomeric R386A THOV NP mutant displays reduced RNA-binding affinity to a 24mer polyU RNA in ITC binding experiments with a K_D = 1400 ± 600 nM, n = 0.95 ± 0.05 compared to K_D = 130 ± 20 nM, n = 0.80 ± 0.01 for WT. Reported errors represent standard deviations of the fit.

(G) THOV NP tail loop mutants analyzed in the polymerase reconstitution assay as described in Figure 2G and western blot analysis of the individual NP tail loop mutants. Shown are mean ± SD of three independent experiments. See also Figure S3.

Please cite this article in press as: Dick et al., Structural characterization of Thogoto Virus nucleoprotein provides insights into viral RNA encapsidation and RNP assembly, Structure (2024), https://doi.org/10.1016/j.str.2024.04.016

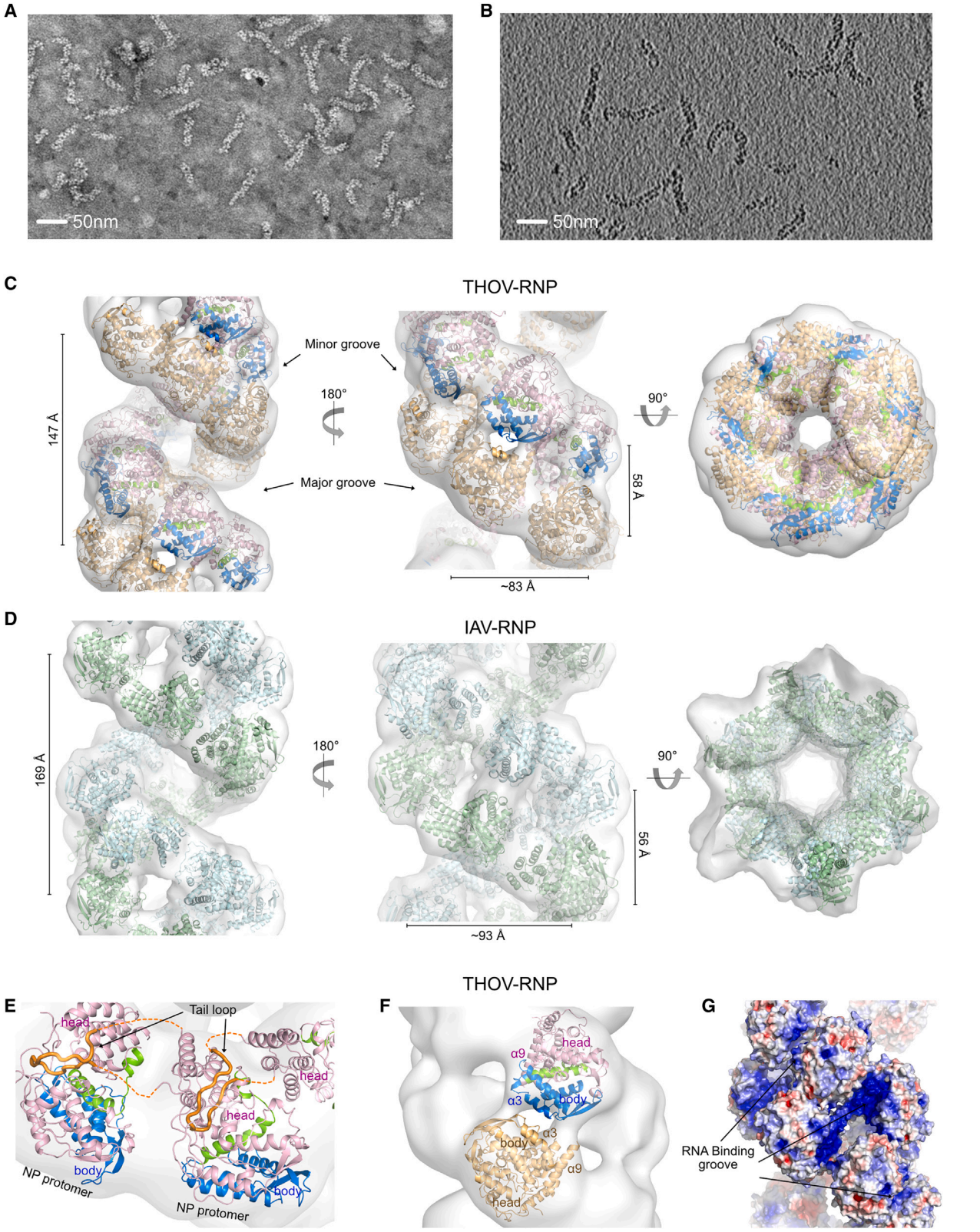

(legend on next page)

Please cite this article in press as: Dick et al., Structural characterization of Thogoto Virus nucleoprotein provides insights into viral RNA encapsidation and RNP assembly, Structure (2024), https://doi.org/10.1016/j.str.2024.04.016

oligomerization plays a role in promoting high-affinity interaction with RNA.

All tested mutations in the tail loop and its binding pocket abolished viral transcriptional activity in the polymerase reconstitution assay (Figure 3G). Our results indicate an essential role of the tail loop for THOV NP oligomerization and transcriptionally active RNPs.

Similar to THOV NP, the mainly positively charged tail loop mediates dimerization in ISAV NP, trimerization in IAV NP, and tetramerization in IBV and IDV NPs via similarly sized interfaces (Figure S3).[18–20,28] Electrostatic surface potential representations indicate that the tip of the THOV NP tail loop contains more positively charged residues as compared to the IAV, IBV, IDV, and ISAV NPs, which feature hydrophobic residues in this region (Figure S3).

Structure of native THOV RNPs from cryo-electron tomography data

To obtain mechanistic insights into viral RNA encapsidation by NP, cryo-ET and sub-tomogram averaging (STA) were performed on THOV RNPs purified from THOV virions.[29] Visual inspection of the RNPs under negative stain or cryo conditions indicated a highly flexible morphology, with straight and bent double-helical structures (Figures 4A and 4B), similar to those of IAV RNPs. A cryo-ET processing pipeline (Figure S4A) produced an STA map of the RNPs at ~17.8 Å (Table S4).

Because of the risk that the hand of the reconstructed tomograms can unintentionally be inverted during the individual steps of the cryo-ET workflow, we employed two strategies to validate the handedness of the resulting STA structures.[30] First, we measured defocus values in tilt series at both sides relative to the tilt axis, which allowed us to unambiguously determine the handedness of the tomograms (Figure S4C).[31] In this way, we identified a left-handed helical assembly of the THOV RNP. Moreover, a small dataset of nine tilt series of purified ribosome large subunit (LSU) was recorded on the same microscope and subjected to the same standardized processing pipeline (Table S4). The resulting map at 9 Å resolution was interpretable with an available LSU structure (PDB: 6LSS) only at one handedness, thereby independently confirming our workflow (Figures S4D–S4F).

The left-handed THOV RNP map of the central region features a double helical structure with a minor groove between connected NP strands and a major groove separating the double strands along the helix (Figure 4C). Density for individual NPs could clearly be distinguished in the map. However, an unequivocal fitting of the NP monomer structures was not possible at this resolution. We, therefore, based our fitting on an AlphaFold prediction of the hexameric NP ring structure, followed by a rigid body fitting (see STAR Methods). Accordingly, the THOV RNP helix is formed by twelve NP monomers per turn comprising six pairs, with a helical rise per monomer of 24.6 Å and a rotation angle (twist) between monomers of −55.5° (Figure S4A), resulting in a turn length (rise) and width of 147 Å and 83 Å, respectively (Figure 4C). The negative value in twist corresponds to a left-handed helix.

Our overall THOV RNP organization is comparable to that of IAV RNP from Arranz and colleagues, with the same number of NP molecules per turn.[22] However, IAV RNPs show slightly different helical parameters of −57° to −64° twist and 28 Å rise, which yield a turn length and width of 169 Å and 93 Å, respectively (Figure 4D). These differences result in a more elongated IAV RNP structure with a larger diameter compared to the THOV RNP (Figures 4C and 4D).

The placement of the THOV$^{\Delta 188\text{-}196}$ NP structure into the STA map revealed that the NP head domains mediate intra-strand contacts between adjacent NP protomers (Figures 4C and 4E), whereas the body domains of the NPs point toward the minor groove and make inter-strand contacts to each other via helices α3 and α9, with a distance of 58 Å (Figures 4C and 4F). This orientation differs from the arrangement of the NP molecules in the IAV RNP structure provided by Arranz et al. due to a ~90° rotation and ~20 Å translation along the rotation axis of the adjacent NP molecules within one strand (Figure S5A).[22]

The proposed NP intra-strand connection via the tail loop was manually adjusted so that it could reach its neighboring binding pocket, as found in the trimeric THOV$^{\Delta 188\text{-}196}$ NP structure (Figure 4E). However, the NP molecule arrangement in the helical THOV RNP structure differs from the trimeric arrangement in the crystal structure by a 98° rotation (Figure S5B).

Due to the low resolution of the cryo-ET map, no RNA was modeled around the RNP strands. However, we propose an antiparallel wrapping of RNA along the two individual RNP strands at the inside of the RNP, as inferred from the electrostatic surface potential of the docked NP monomers, the phosphate ions detected in the positively charged groove indicating a possible RNA backbone interaction, from our RNA-binding mutants and a comparison with an RNA-containing IAV RNP structures (Figures 2B, 4G, S5C, and S5D).[26,32]

Figure 4. Structure of THOV RNP and comparison to IAV RNP

Purified THOV RNPs in uranyl acetate negative stain (A) or monitored by cryo-EM (B). The scale bar is 50 nm.

(C) Side and top views of the reconstructed STA map with 16 fitted NP subunits of the central part of the THOV RNP show two strands running in opposite directions. The two strands are shown as cartoon structures in orange and NP domain-defining colors blue, pink, and green for the body, head, and helix-loop-helix motif, respectively. The size specifications result from measurements based on the distances between the centers of mass (COM) of the corresponding NP subunits.

(D) Three-side views of the central, helical IAV-RNP part taken from ref.[22] (PDB: 4BBL, EMDB: EMD-2205) with the fitted double NP strands shown as light blue and light green cartoon structures. The views are oriented as in (C) for comparison with their corresponding COM distance measurements.

(E) Top view of neighboring NP protomers showing the intra-strand connections via the tail loops. The NP protomers are depicted as cartoon representations with their body and head domains colored in blue and pink, respectively, and the helix-loop-helix motif in green. The swapping tail loop is modeled into the adjacent molecule and is highlighted in orange.

(F) Docking of two NP protomers showing inter-strand connections mediated by helix α3 of each NP molecule.

(G) The electrostatic surface potential of the THOV RNP central part reveals positively charged RNA binding grooves within the NP strands. The color ranges from −5 kcal/mol*e in red to +5 kcal/mol*e in blue. The putative RNA binding area is further illustrated in Figure S5D. See also Figures S4 and S5, Tables S1 and S4.

Please cite this article in press as: Dick et al., Structural characterization of Thogoto Virus nucleoprotein provides insights into viral RNA encapsidation and RNP assembly, Structure (2024), https://doi.org/10.1016/j.str.2024.04.016

DISCUSSION

Thogotoviruses are a group of tick-borne orthomyxoviruses with a morphology and genetic architecture similar to influenza viruses.[3] In the present study, we determined the high-resolution crystal structure of the trimeric THOV NP and a low-resolution cryo-ET map of the native THOV RNP. Our structural analyses indicate that the NP of THOV and influenza viruses share a related three-dimensional architecture, including related head and body domains. Also, the putative RNA-binding groove along the interface between the two domains is at similar positions. Furthermore, we demonstrate that similar to influenza viruses, THOV oligomerization proceeds through a tail loop, also referred to as the "oligomerization-loop".[32] Finally, our cryo-ET reconstruction of native THOV RNPs yields a model that is consistent with one of the previously described RNP models of IAV.[22] Our structural analyses suggest that IAV and THOV RNPs employ related oligomerization and RNA encapsidation modes, which are detailed in the following paragraphs.

We employed ITC for our RNA-binding studies with THOV NP, offering the advantage of working with reactants in their native state, e.g., without modification or immobilization, yielding a K_D in the high nanomolar range to a 24-mer RNA (K_D = 130 nM). Based on previous fluorescence anisotropy experiments, the interaction of IAV and IBV NP with RNA depends on RNA length and salt concentration.[33] At physiological pH and using a 24-mer RNA, K_Ds of 4 nM and 69 nM were determined for IAV and IBV NPs, respectively. Similar affinities in the low nanomolar range were observed for IAV NP binding to a 28-mer RNA sequence using surface plasmon resonance experiments.[34] The observed differences in binding strength may relate to the different methods or the less positively charged RNA-binding groove in THOV NP compared to IAV (Figure S2). Also, the different RNA sequences used in the three mentioned studies may contribute to variations in binding affinities. In native IAV RNP, each NP binds about 26 RNA bases.[35] Some bases were shown to be accommodated directly in the RNA-binding groove between the head and body domain,[26] as we have also demonstrated by mutagenesis for THOV NP. However, parts of the RNA may be sequestered between two adjacent NPs,[32] which is consistent with our THOV RNP model.

We show that the conserved tail loop has a fundamental function in the assembly of THOV NPs by allowing the assembly into a trimer at physiological salt concentrations. IAV NP assembles into a trimer at higher salt concentrations (300 mM), whereas it exists in equilibrium between monomers and trimers at lower salt concentrations (50 mM and 150 mM).[33] Other influenazvirus NPs also employ a tail loop for their assembly into dimers, trimers, or tetramers (Figure 3). NP-NP interaction is primarily mediated by positively charged residues of the tail loop which bind into a negatively charged pocket formed by elements of the head and body domain (Figure 3C). This interaction typically includes a strictly conserved arginine residue in the tail loop making a salt bridge to a strictly conserved glutamate in its binding pocket, as also found in THOV NP. Truncation of the tail loop or mutation of the conserved Arg386 to alanine in THOV NP resulted in the loss of the trimeric in favor of the monomeric form (Figure 3E). In addition, the R386A mutant bound with a 10-fold reduced affinity to polyU 24-mer RNA compared to the WT NP trimer, suggesting a coupling of NP oligomerization and RNA binding (Figure 3F). Our results are in line with the observation made for IAV NP, where the alanine mutant of the conserved Arg416 showed loss of trimerization toward a monomer, combined with reduced RNA binding due to a reorientation of the tail loop, now interacting with alternative sites on the monomer surface that compete with RNA binding.[36] The decreased RNA binding of the THOV NP oligomerization defective R386A tail loop mutant suggests a similar mechanism for the unbound THOV NP tail loop.

In line with our minireplicon data and with a recent cryo-EM structure of a reconstituted IAV RNP,[32] the tail loop also mediates NP protomer connections within the RNP. Interestingly, adjacent NP molecules undergo a drastic rearrangement when comparing the trimeric NP with the RNP model, which is facilitated by the high flexibility of the tail loop (Figure S5B). This flexibility may also allow oligomerization of the NP molecules into left- or right-handed RNP helices, e.g., by a rotation of the NP molecules of ~70° (Figure S5E).[22,23,32]

A putative error source for determining the correct handedness of a cryo-electron tomogram is a 180° ambiguity in the determination of the tilt axis in a tilt series. To establish the handedness of THOV RNP, we determined defocus values on both sides of the tilt axis, thereby identifying a left-handed helical assembly of the THOV RNP cryo-ET reconstruction.[31] Based on the resulting STA density, we propose a THOV RNP model related to the IAV RNP model of Arranz and colleagues: NPs assemble head-to-tail to form a single, polar NP filament, while a second NP filament co-assembles in an antiparallel fashion, yielding a double helical antiparallel assembly. The contact between the two strands in our model is mediated by the body domain's N-terminal helix α3 and the head domain helix α9, which face the same helix or the diagonally adjacent helix in the opposite NP molecule. Interestingly, for IAV RNP, both left- and right-handed assemblies were described. A right-handed assembly was confirmed by atomic force microscopy-based studies for virion-derived IAV RNPs[37] and for a reconstituted IAV RNP-like structure with a short RNA oligomer.[32] A right-handed viral IAV miniRNP[24] and the two left-handed native IAV RNP structures[22,38] were validated by cryo-EM based procedures.

A detailed modeling of the RNA bound to the THOV RNPs was not possible at the current resolution. However, based on the different orientation of the NP molecules in the THOV RNP compared to the NP arrangement in the IAV RNP structure from Arranz et al. (Figure S5A), the position of the positively charged RNA binding groove differs in the two models.[22] We assume that the RNA wraps along the individual THOV NP molecules at the positively charged inner side cavity of each filament strand (Figures 4G, S5C, and S5D). In contrast, Arranz et al. proposed a meandering path of the RNA molecule in IAV. The detailed identification of the RNA path bound to the native RNPs of THOV awaits further clarification by future high-resolution structural studies.

Higher resolution information is also needed to better assess the contribution of the different interfaces and conformational changes in THOV NP required for its oligomerization and incorporation into the RNP structure. However, the high flexibility of the orthomyxoviral RNPs imposes problems on their advanced structural characterization.[23] High flexibility in RNP

conformations was also detected for other ssRNA viruses, such as orthobunyaviruses, and is likely a result of the small interaction interfaces between the NP protomers across the longitudinal axis of the RNPs.[39] For other negative-sense ssRNA viruses with a larger NP interface and/or a tighter NP packaging, high-resolution structures of RNPs have been described, e.g., mumps virus,[40,41] Ebola virus,[42] Nipah virus,[43] or Hantaan virus.[44] Engineering orthomyxovirus RNPs with increased stability may be a suitable strategy for future high-resolution cryo-EM studies.

Well-diffracting crystals of THOV NP could only be obtained by deleting residues 188–196, forming an exposed loop that contains a nuclear localization signal (NLS).[45] Based on the present crystal structure of the THOV NP trimer, the NLS is exposed and accessible for the nuclear import machinery, e.g., importin-α. Intriguingly, in our THOV RNP helical model, the NLS is buried inside the RNP oligomer and inaccessible to the nuclear import machinery. Accordingly, we would speculate that this NLS loop may act as a molecular switch, regulating intracellular trafficking of NP in THOV-infected cells. The newly synthesized monomeric or trimeric NP would be qualified for nuclear import by the exposed NLS. Upon subsequent replication of the viral genome and assembly of the NPs into mature RNP structures in the nuclear compartment, the NP is now unable to bind importins and may therefore be disposed for interaction with components of the nuclear export machinery. The newly assembled RNPs are then exported into the cytoplasm and travel to the plasma membrane, leading to the final budding of new viral progeny, as summarized recently for thogoto- and influenza viruses.[3,13]

Due to their potential to cause worldwide epidemics, zoonotic viruses have obtained increased attention in recent years. Owing to its potential for genetic reassortment and the fatal consequences of infection to humans and animals, thogotoviruses constitute a serious threat to human and animal health. Accordingly, strategies for antiviral treatment options are desirable because of potential epidemic outbreaks. While most of the available directly acting antiviral drugs target enzymatic activities of viral proteases and polymerases, NPs are becoming increasingly promising targets for the development of antivirals that interfere with structural functions, like the RNA-binding groove or the tail loop pocket. Our high-resolution structure of the THOV NP may provide the structural basis for the design of such antivirals against thogoto- and other orthomyxoviruses.

STAR★METHODS

Detailed methods are provided in the online version of this paper and include the following:

- KEY RESOURCES TABLE
- RESOURCE AVAILABILITY
  - Lead contact
  - Materials availability
  - Data and code availability
- EXPERIMENTAL MODEL AND STUDY PARTICIPANT DETAILS
- METHOD DETAILS
  - Protein expression and purification
  - Analytical gel filtration
  - Analytical ultracentrifugation
  - Right angle laser scattering (RALS)
  - Crystallization and data collection
  - Atomic model building and refinement
  - Grid preparation and image acquisition for cryo-ET
  - THOV-RNP tomogram reconstruction and subtomogram averaging
  - Validation of the handedness of STA structures
  - RNA-binding studies
  - Polymerase reconstitution assay
  - Immunoblot analysis
- QUANTIFICATION AND STATISTICAL ANALYSIS

SUPPLEMENTAL INFORMATION

Supplemental information can be found online at https://doi.org/10.1016/j.str.2024.04.016.

ACKNOWLEDGMENTS

This work was supported by grants from the German Research Foundation (DA 1127/1-2 and SFB958/A12 to O.D. and KO 1579/12-1 to G.K.). We would like to thank the staff of BESSY 2 and PETRA 3 beamline P11 for their support in X-ray data collection. Access to BESSY 2 BL14.1 was granted via the Joint Berlin MX-Laboratory. The Core Facility for cryo-EM (CFcryoEM) of the Charité-Universitätsmedizin Berlin was supported by the German Research Foundation through grant no. INST 335/588-1 FUGG.

AUTHOR CONTRIBUTIONS

A.D. cloned, purified, and crystallized protein constructs, collected X-ray data, built an initial model, and performed biochemical experiments. V.M. processed the cryo-ET data. F.K. prepared grids and assisted in data collection. J.F. and E.B. performed the polymerase reconstitution assays. D.O. assisted in X-ray data acquisition and processing. T.S. and C.D. performed cryo-ET data collection and assisted in structure solution. G.K. and O.D. supervised the project. O.D. assisted in model building. Y.R. grew crystals, solved the final X-ray structure, finished model building, and performed NP model fitting and refinement into the STA map. A.D., Y.R., and O.D. wrote the article, with inputs from all authors.

DECLARATION OF INTERESTS

The authors declare no competing interests.

Received: March 14, 2023
Revised: March 11, 2024
Accepted: April 18, 2024
Published: May 14, 2024

REFERENCES

1. Walker, P.J., Siddell, S.G., Lefkowitz, E.J., Mushegian, A.R., Adriaenssens, E.M., Alfenas-Zerbini, P., Dempsey, D.M., Dutilh, B.E., García, M.L., Curtis Hendrickson, R., et al. (2022). Recent changes to virus taxonomy ratified by the International Committee on Taxonomy of Viruses (2022). Arch. Virol. *167*, 2429–2440. https://doi.org/10.1007/s00705-022-05516-5.
2. McCauley, J., Hongo, S., Kaverin, N., Kochs, G., Lamb, R., Matrosovich, M., Perez, D., Palese, P., Presti, R., and Rimstad, E. (2012). Family Orthomyxoviridae. Virus Taxonomy: Ninth Report of the International Committee on Taxonomy of Viruses, pp. 749–761.
3. Bendl, E., Fuchs, J., and Kochs, G. (2023). Bourbon virus, a newly discovered zoonotic thogotovirus. J. Gen. Virol. *104*. https://doi.org/10.1099/jgv.0.001887.
4. Krammer, F., Smith, G.J.D., Fouchier, R.A.M., Peiris, M., Kedzierska, K., Doherty, P.C., Palese, P., Shaw, M.L., Treanor, J., Webster, R.G., and García-Sastre, A. (2018). Influenza. Nat. Rev. Dis. Prim. *4*, 3. https://doi.org/10.1038/s41572-018-0002-y.
5. Kosoy, O.I., Lambert, A.J., Hawkinson, D.J., Pastula, D.M., Goldsmith, C.S., Hunt, D.C., and Staples, J.E. (2015). Novel thogotovirus associated

with febrile illness and death, United States, 2014. Emerg. Infect. Dis. *21*, 760–764. https://doi.org/10.3201/eid2105.150150.

6. Tran, N.T.B., Shimoda, H., Ishijima, K., Yonemitsu, K., Minami, S., Supriyono, Kuroda, Y., Tatemoto, K., Mendoza, M.V., Kuwata, R., et al. (2022). Zoonotic Infection with Oz Virus, a Novel Thogotovirus. Emerg. Infect. Dis. *28*, 436–439. https://doi.org/10.3201/eid2802.211270.
7. Bricker, T.L., Shafiuddin, M., Gounder, A.P., Janowski, A.B., Zhao, G., Williams, G.D., Jagger, B.W., Diamond, M.S., Bailey, T., Kwon, J.H., et al. (2019). Therapeutic efficacy of favipiravir against Bourbon virus in mice. PLoS Pathog. *15*, e1007790. https://doi.org/10.1371/journal.ppat.1007790.
8. Davies, F.G., Soi, R.K., and Wariru, B.N. (1984). Abortion in sheep caused by Thogoto virus. Vet. Rec. *115*, 654. https://doi.org/10.1136/vr.115.25-26.654.
9. Filipe, A.R., Peleteiro, M.C., Monath, T.M., and Calisher, E.H. (1986). Pathological lesions in mice infected with Thogoto virus, a tick-borne orthomyxovirus. Acta Virol. *30*, 337–340.
10. Mateo, R.I., Xiao, S.Y., Lei, H., DA Rosa, A.P.A.T., and Tesh, R.B. (2007). Dhori virus (Orthomyxoviridae: Thogotovirus) infection in mice: a model of the pathogenesis of severe orthomyxovirus infection. Am. J. Trop. Med. Hyg. *76*, 785–790.
11. Fuchs, J., Lamkiewicz, K., Kolesnikova, L., Hölzer, M., Marz, M., and Kochs, G. (2022). Comparative Study of Ten Thogotovirus Isolates and Their Distinct In Vivo Characteristics. J. Virol. *96*, e0155621. https://doi.org/10.1128/jvi.01556-21.
12. Guilligay, D., Kadlec, J., Crépin, T., Lunardi, T., Bouvier, D., Kochs, G., Ruigrok, R.W.H., and Cusack, S. (2014). Comparative structural and functional analysis of orthomyxovirus polymerase cap-snatching domains. PLoS One *9*, e84973. https://doi.org/10.1371/journal.pone.0084973.
13. Eisfeld, A.J., Neumann, G., and Kawaoka, Y. (2015). At the centre: influenza A virus ribonucleoproteins. Nat. Rev. Microbiol. *13*, 28–41. https://doi.org/10.1038/nrmicro3367.
14. Portela, A., and Digard, P. (2002). The influenza virus nucleoprotein: a multifunctional RNA-binding protein pivotal to virus replication. J. Gen. Virol. *83*, 723–734. https://doi.org/10.1099/0022-1317-83-4-723.
15. Green, T.J., and Luo, M. (2009). Structure of the vesicular stomatitis virus nucleocapsid in complex with the nucleocapsid-binding domain of the small polymerase cofactor, P. Proc. Natl. Acad. Sci. USA *106*, 11713–11718. https://doi.org/10.1073/pnas.0903228106.
16. Albertini, A.A.V., Wernimont, A.K., Muziol, T., Ravelli, R.B.G., Clapier, C.R., Schoehn, G., Weissenhorn, W., and Ruigrok, R.W.H. (2006). Crystal structure of the rabies virus nucleoprotein-RNA complex. Science *313*, 360–363. https://doi.org/10.1126/science.1125280.
17. Reguera, J., Cusack, S., and Kolakofsky, D. (2014). Segmented negative strand RNA virus nucleoprotein structure. Curr. Opin. Virol. *5*, 7–15. https://doi.org/10.1016/j.coviro.2014.01.003.
18. Ng, A.K.L., Zhang, H., Tan, K., Li, Z., Liu, J.H., Chan, P.K.S., Li, S.M., Chan, W.Y., Au, S.W.N., Joachimiak, A., et al. (2008). Structure of the influenza virus A H5N1 nucleoprotein: implications for RNA binding, oligomerization, and vaccine design. Faseb. J. *22*, 3638–3647. https://doi.org/10.1096/fj.08-112110.
19. Ye, Q., Krug, R.M., and Tao, Y.J. (2006). The mechanism by which influenza A virus nucleoprotein forms oligomers and binds RNA. Nature *444*, 1078–1082. https://doi.org/10.1038/nature05379.
20. Donchet, A., Oliva, J., Labaronne, A., Tengo, L., Miloudi, M., C A Gerard, F., Mas, C., Schoehn, G., W H Ruigrok, R., Ducatez, M., and Crépin, T. (2019). The structure of the nucleoprotein of Influenza D shows that all Orthomyxoviridae nucleoproteins have a similar NP(CORE), with or without a NP(TAIL) for nuclear transport. Sci. Rep. *9*, 600. https://doi.org/10.1038/s41598-018-37306-y.
21. Zheng, W., Olson, J., Vakharia, V., and Tao, Y.J. (2013). The crystal structure and RNA-binding of an orthomyxovirus nucleoprotein. PLoS Pathog. *9*, e1003624. https://doi.org/10.1371/journal.ppat.1003624.
22. Arranz, R., Coloma, R., Chichón, F.J., Conesa, J.J., Carrascosa, J.L., Valpuesta, J.M., Ortín, J., and Martín-Benito, J. (2012). The structure of native influenza virion ribonucleoproteins. Science *338*, 1634–1637. https://doi.org/10.1126/science.1228172.
23. Coloma, R., Arranz, R., de la Rosa-Trevín, J.M., Sorzano, C.O.S., Munier, S., Carlero, D., Naffakh, N., Ortín, J., and Martín-Benito, J. (2020). Structural insights into influenza A virus ribonucleoproteins reveal a processive helical track as transcription mechanism. Nat. Microbiol. *5*, 727–734. https://doi.org/10.1038/s41564-020-0675-3.
24. Moeller, A., Kirchdoerfer, R.N., Potter, C.S., Carragher, B., and Wilson, I.A. (2012). Organization of the influenza virus replication machinery. Science *338*, 1631–1634. https://doi.org/10.1126/science.1227270.
25. Tarus, B., Chevalier, C., Richard, C.A., Delmas, B., Di Primo, C., and Slama-Schwok, A. (2012). Molecular dynamics studies of the nucleoprotein of influenza A virus: role of the protein flexibility in RNA binding. PLoS One *7*, e30038. https://doi.org/10.1371/journal.pone.0030038.
26. Tang, Y.S., Xu, S., Chen, Y.W., Wang, J.H., and Shaw, P.C. (2021). Crystal structures of influenza nucleoprotein complexed with nucleic acid provide insights into the mechanism of RNA interaction. Nucleic Acids Res. *49*, 4144–4154. https://doi.org/10.1093/nar/gkab203.
27. Tarus, B., Bakowiez, O., Chenavas, S., Duchemin, L., Estrozi, L.F., Bourdieu, C., Lejal, N., Bernard, J., Moudjou, M., Chevalier, C., et al. (2012). Oligomerization paths of the nucleoprotein of influenza A virus. Biochimie *94*, 776–785. https://doi.org/10.1016/j.biochi.2011.11.009.
28. Ng, A.K.L., Lam, M.K.H., Zhang, H., Liu, J., Au, S.W.N., Chan, P.K.S., Wang, J., and Shaw, P.C. (2012). Structural basis for RNA binding and homo-oligomer formation by influenza B virus nucleoprotein. J. Virol. *86*, 6758–6767. https://doi.org/10.1128/jvi.00073-12.
29. Kochs, G., and Haller, O. (1999). Interferon-induced human MxA GTPase blocks nuclear import of Thogoto virus nucleocapsids. Proc. Natl. Acad. Sci. USA *96*, 2082–2086. https://doi.org/10.1073/pnas.96.5.2082.
30. Briegel, A., Pilhofer, M., Mastronarde, D.N., and Jensen, G.J. (2013). The challenge of determining handedness in electron tomography and the use of DNA origami gold nanoparticle helices as molecular standards. J. Struct. Biol. *183*, 95–98. https://doi.org/10.1016/j.jsb.2013.04.008.
31. Mindell, J.A., and Grigorieff, N. (2003). Accurate determination of local defocus and specimen tilt in electron microscopy. J. Struct. Biol. *142*, 334–347. https://doi.org/10.1016/s1047-8477(03)00069-8.
32. Chenavier, F., Estrozi, L.F., Teulon, J.M., Zarkadas, E., Freslon, L.L., Pellequer, J.L., Ruigrok, R.W.H., Schoehn, G., Ballandras-Colas, A., and Crépin, T. (2023). Cryo-EM structure of influenza helical nucleocapsid reveals NP-NP and NP-RNA interactions as a model for the genome encapsidation. Sci. Adv. *9*, eadj9974. https://doi.org/10.1126/sciadv.adj9974.
33. Labaronne, A., Swale, C., Monod, A., Schoehn, G., Crépin, T., and Ruigrok, R.W.H. (2016). Binding of RNA by the Nucleoproteins of Influenza Viruses A and B. Viruses *8*, 247. https://doi.org/10.3390/v8090247.
34. Liu, C.L., Hung, H.C., Lo, S.C., Chiang, C.H., Chen, I.J., Hsu, J.T.A., and Hou, M.H. (2016). Using mutagenesis to explore conserved residues in the RNA-binding groove of influenza A virus nucleoprotein for antiviral drug development. Sci. Rep. *6*, 21662. https://doi.org/10.1038/srep21662.
35. Ortega, J., Martín-Benito, J., Zürcher, T., Valpuesta, J.M., Carrascosa, J.L., and Ortín, J. (2000). Ultrastructural and functional analyses of recombinant influenza virus ribonucleoproteins suggest dimerization of nucleoprotein during virus amplification. J. Virol. *74*, 156–163.
36. Chenavas, S., Estrozi, L.F., Slama-Schwok, A., Delmas, B., Di Primo, C., Baudin, F., Li, X., Crépin, T., and Ruigrok, R.W.H. (2013). Monomeric nucleoprotein of influenza A virus. PLoS Pathog. *9*, e1003275. https://doi.org/10.1371/journal.ppat.1003275.
37. Nakano, M., Sugita, Y., Kodera, N., Miyamoto, S., Muramoto, Y., Wolf, M., and Noda, T. (2021). Ultrastructure of influenza virus ribonucleoprotein complexes during viral RNA synthesis. Commun. Biol. *4*, 858. https://doi.org/10.1038/s42003-021-02388-4.

38. Coloma, R., Valpuesta, J.M., Arranz, R., Carrascosa, J.L., Ortín, J., and Martín-Benito, J. (2009). The structure of a biologically active influenza virus ribonucleoprotein complex. PLoS Pathog. *5*, e1000491. https://doi.org/10.1371/journal.ppat.1000491.

39. Hopkins, F.R., Álvarez-Rodríguez, B., Heath, G.R., Panayi, K., Hover, S., Edwards, T.A., Barr, J.N., and Fontana, J. (2021). The structure of a native orthobunyavirus ribonucleoprotein reveals a key role for viral RNA in maintaining its helical architecture. Preprint at bioRxiv. https://doi.org/10.1101/2021.10.27.466080.

40. Shan, H., Su, X., Li, T., Qin, Y., Zhang, N., Yang, L., Ma, L., Bai, Y., Qi, L., Liu, Y., and Shen, Q.T. (2021). Structural plasticity of mumps virus nucleocapsids with cryo-EM structures. Commun. Biol. *4*, 833. https://doi.org/10.1038/s42003-021-02362-0.

41. Zhang, X., Sridharan, S., Zagoriy, I., Oegema, C.E., Ching, C., Pflaesterer, T., Fung, H.K.H., Poser, I., Müller, C.W., Hyman, A.A., et al. (2022). Molecular mechanisms of stress-induced reactivation in mumps virus condensates. Preprint at bioRxiv. https://doi.org/10.1101/2021.07.10.451879.

42. Kirchdoerfer, R.N., Saphire, E.O., and Ward, A.B. (2019). Cryo-EM structure of the Ebola virus nucleoprotein-RNA complex. Acta Crystallogr. F Struct. Biol. Commun. *75*, 340–347. https://doi.org/10.1107/s2053230x19004424.

43. Ker, D.S., Jenkins, H.T., Greive, S.J., and Antson, A.A. (2021). CryoEM structure of the Nipah virus nucleocapsid assembly. PLoS Pathog. *17*, e1009740. https://doi.org/10.1371/journal.ppat.1009740.

44. Arragain, B., Reguera, J., Desfosses, A., Gutsche, I., Schoehn, G., and Malet, H. (2019). High resolution cryo-EM structure of the helical RNA-bound Hantaan virus nucleocapsid reveals its assembly mechanisms. Elife *8*, e43075. https://doi.org/10.7554/eLife.43075.

45. Weber, F., Kochs, G., Gruber, S., and Haller, O. (1998). A classical bipartite nuclear localization signal on Thogoto and influenza A virus nucleoproteins. Virology *250*, 9–18. https://doi.org/10.1006/viro.1998.9329.

46. Schuck, P. (2000). Size-distribution analysis of macromolecules by sedimentation velocity ultracentrifugation and lamm equation modeling. Biophys. J. *78*, 1606–1619. https://doi.org/10.1016/S0006-3495(00)76713-0.

47. Laue, T., Shah, B., Ridgeway, T., Pelletier, S., Harding, S., Rowe, A., and Horton, J. (1992). Analytical Ultracentrifugation in Biochemistry and Polymer Science (Royal Society of Chemistry).

48. Sheldrick, G.M. (2008). A short history of SHELX. Acta Crystallogr. A *64*, 112–122. https://doi.org/10.1107/S0108767307043930.

49. Pape, T., and Schneider, T.R. (2004). HKL2MAP: a graphical user interface for macromolecular phasing with SHELX programs. J. Appl. Crystallogr. *37*, 843–844. https://doi.org/10.1107/S0021889804018047.

50. Emsley, P., and Cowtan, K. (2004). Coot: model-building tools for molecular graphics. Acta Crystallogr. D Biol. Crystallogr. *60*, 2126–2132. https://doi.org/10.1107/S0907444904019158.

51. McCoy, A.J., Grosse-Kunstleve, R.W., Adams, P.D., Winn, M.D., Storoni, L.C., and Read, R.J. (2007). Phaser crystallographic software. J. Appl. Crystallogr. *40*, 658–674. https://doi.org/10.1107/s0021889807021206.

52. Afonine, P.V., Poon, B.K., Read, R.J., Sobolev, O.V., Terwilliger, T.C., Urzhumtsev, A., and Adams, P.D. (2018). Real-space refinement in PHENIX for cryo-EM and crystallography. Acta Crystallogr. D Struct. Biol. *74*, 531–544. https://doi.org/10.1107/s2059798318006551.

53. Ashkenazy, H., Abadi, S., Martz, E., Chay, O., Mayrose, I., Pupko, T., and Ben-Tal, N. (2016). ConSurf 2016: an improved methodology to estimate and visualize evolutionary conservation in macromolecules. Nucleic Acids Res. *44*, W344–W350. https://doi.org/10.1093/nar/gkw408.

54. Pettersen, E.F., Goddard, T.D., Huang, C.C., Couch, G.S., Greenblatt, D.M., Meng, E.C., and Ferrin, T.E. (2004). UCSF Chimera–a visualization system for exploratory research and analysis. J. Comput. Chem. *25*, 1605–1612. https://doi.org/10.1002/jcc.20084.

55. Mastronarde, D.N. (2005). Automated electron microscope tomography using robust prediction of specimen movements. J. Struct. Biol. *152*, 36–51. https://doi.org/10.1016/j.jsb.2005.07.007.

56. Hagen, W.J.H., Wan, W., and Briggs, J.A.G. (2017). Implementation of a cryo-electron tomography tilt-scheme optimized for high resolution subtomogram averaging. J. Struct. Biol. *197*, 191–198. https://doi.org/10.1016/j.jsb.2016.06.007.

57. Balyschew, N., Yushkevich, A., Mikirtumov, V., Sanchez, R.M., Sprink, T., and Kudryashev, M. (2023). Streamlined structure determination by cryo-electron tomography and subtomogram averaging using TomoBEAR. Nat. Commun. *14*, 6543. https://doi.org/10.1038/s41467-023-42085-w.

58. Zheng, S.Q., Palovcak, E., Armache, J.P., Verba, K.A., Cheng, Y., and Agard, D.A. (2017). MotionCor2: anisotropic correction of beam-induced motion for improved cryo-electron microscopy. Nat. Methods *14*, 331–332. https://doi.org/10.1038/nmeth.4193.

59. Zheng, S., Wolff, G., Greenan, G., Chen, Z., Faas, F.G.A., Bárcena, M., Koster, A.J., Cheng, Y., and Agard, D.A. (2022). AreTomo: An integrated software package for automated marker-free, motion-corrected cryo-electron tomographic alignment and reconstruction. J. Struct. Biol. X *6*, 100068. https://doi.org/10.1016/j.yjsbx.2022.100068.

60. Zhang, K. (2016). Gctf: Real-time CTF determination and correction. J. Struct. Biol. *193*, 1–12. https://doi.org/10.1016/j.jsb.2015.11.003.

61. Castaño-Díez, D., Kudryashev, M., Arheit, M., and Stahlberg, H. (2012). Dynamo: a flexible, user-friendly development tool for subtomogram averaging of cryo-EM data in high-performance computing environments. J. Struct. Biol. *178*, 139–151. https://doi.org/10.1016/j.jsb.2011.12.017.

62. Kimanius, D., Dong, L., Sharov, G., Nakane, T., and Scheres, S.H.W. (2021). New tools for automated cryo-EM single-particle analysis in RELION-4.0. Biochem. J. *478*, 4169–4185. https://doi.org/10.1042/bcj20210708.

63. Zivanov, J., Otón, J., Ke, Z., von Kügelgen, A., Pyle, E., Qu, K., Morado, D., Castaño-Díez, D., Zanetti, G., Bharat, T.A.M., et al. (2022). A Bayesian approach to single-particle electron cryo-tomography in RELION-4.0. Elife *11*, e83724. https://doi.org/10.7554/eLife.83724.

64. Albanese, M., Bruno-Smiraglia, C., Di di Cuonzo, G., Lavagnino, A., and Srihongse, S. (1972). Isolation of Thogoto virus from Rhipicephalus bursa ticks in western Sicily. Acta Virol. *16*, 267.

65. Niwa, H., Yamamura, K., and Miyazaki, J. (1991). Efficient selection for high-expression transfectants with a novel eukaryotic vector. Gene *108*, 193–199. https://doi.org/10.1016/0378-1119(91)90434-d.

66. Patzina, C., Haller, O., and Kochs, G. (2014). Structural requirements for the antiviral activity of the human MxA protein against Thogoto and influenza A virus. J. Biol. Chem. *289*, 6020–6027. https://doi.org/10.1074/jbc.M113.543892.

67. Kochs, G., and Haller, O. (1999). GTP-bound human MxA protein interacts with the nucleocapsids of Thogoto virus (Orthomyxoviridae). J. Biol. Chem. *274*, 4370–4376.

Please cite this article in press as: Dick et al., Structural characterization of Thogoto Virus nucleoprotein provides insights into viral RNA encapsidation and RNP assembly, Structure (2024), https://doi.org/10.1016/j.str.2024.04.016

STAR★METHODS

KEY RESOURCES TABLE

REAGENT or RESOURCE	SOURCE	IDENTIFIER
Antibodies		
Anti-Flag-tag	Sigma	MAB3118; RRID: AB_9470
Anti-HA-tag	Sigma	H3663; RRID: AB_262051
Anti-β-actin	Sigma	A2228; RRID: AB_476697
Anti-Flag-M2 affinity gel	Sigma	A2220; RRID: AB_10063035
Anti-THOV NP Ab	Kochs et al.[67]	N/A
Bacterial and virus strains		
E. coli BL21 (DE3) Rosetta strain	Novagen/Sigma	#70954
THOV, strain SiAr126	Albanese et al.[64]	N/A
Chemicals, peptides, and recombinant proteins		
GST-tagged PreScission™ Protease	This Paper	N/A
Seleno-L-methionine	Sigma	# S3132
Isopropyl-β-D-thiogalactopyranoside (IPTG)	Sigma	10724815001
NP-40 alternative	CalBioChem	492016
Triton X-100	Sigma	93426
Lysolecithin	Sigma	L5254
Deposited data		
THOV NP (delta 188-196) Apo Structure	This Paper	PDB: 8CJW
THOV RNP	This Paper	PDB: 8RYT,EMDB: EMD-19599
Experimental models: Cell lines		
HEK293T cells	ATCC	CRL-3216; RRID: CVCL_0063
Oligonucleotides		
single-stranded RNA of varying length (pU14 - pU24)	This Paper	https://www.idtdna.com/pages/products/custom-dna-rna/custom-rna-oligos
Primer used in this study (Table S5)	This Paper	N/A
Recombinant DNA		
pET28 plasmids (THOV NP constructs)	This Paper	N/A
pCAGGS	Niwa et al.[65]	N/A
pHH21-vNP-FFLuc	Patzina et al.[66]	N/A
pRL-SV40	Promega	E2231
Software and algorithms		
Sedfit	Schuck et al.[46]	https://sedfitsedphat.github.io/
SEDNTERP	Laue et al.[47]	http://www.jphilo.mailway.com/sednterp.htm
Omnisec	No reference available	https://www.malvernpanalytical.com/en/products/product-range/omnisec
SHELXD	Sheldrick et al.[48]	https://www.ccp4.ac.uk/download/shelx.php
HKL2MAP	Pape et al.[49]	https://www.ccp4.ac.uk/schools/APS-2010/tutorials/shelx/tutorial_shelx_chicago2008.pdf
Coot	Emsley et al.[50]	https://www.ccp4.ac.uk/download/#os=windows
Phaser	McCoy et al.[51]	https://www.ccp4.ac.uk/html/phaser.html
Phenix	Afonine et al.[52]	https://phenix-online.org/
PyMOL Molecular Graphics System, Version 2.5.2	Schrödinger	https://pymol.org/
Consurf Server	Ashkenazy et al.[53]	https://consurf.tau.ac.il/consurf_index.php
Chimera	Pettersen et al.[54]	https://www.cgl.ucsf.edu/chimera/

(*Continued on next page*)

Please cite this article in press as: Dick et al., Structural characterization of Thogoto Virus nucleoprotein provides insights into viral RNA encapsidation and RNP assembly, Structure (2024), https://doi.org/10.1016/j.str.2024.04.016

Continued

REAGENT or RESOURCE	SOURCE	IDENTIFIER
Relion 4	Kimanius et al.[62] Zivanov et al.[63]	https://relion.readthedocs.io/en/release-4.0/
IMOD	Mastronarde et al.[55]	https://bio3d.colorado.edu/imod/
Dynamo	Castaño-Díez et al.[61]	https://www.dynamo-em.org//w/index.php?title=Main_Page
Origin Pro	https://www.originlab.com/	https://www.originlab.com/
GraphPad Prism 6	Dotmatics	https://www.graphpad.com/support/updates/?program=Prism&platform=Win&version=6.04
TomoBEAR	Balyschew et al.[57]	https://github.com/KudryashevLab/TomoBEAR
GCTF	Zhang et al.[60]	https://www2.mrc-lmb.cam.ac.uk/download/gctf/
MotionCor2	Zheng et al.[58]	https://emcore.ucsf.edu/ucsf-software
AreTomo	Zheng et al.[59]	https://msg.ucsf.edu/software

RESOURCE AVAILABILITY

Lead contact

Further information and requests for resources and reagents should be directed to and will be fulfilled by the lead contact, Oliver Daumke (oliver.daumke@mdc-berlin.de).

Materials availability

All plasmids generated in this study are available from the lead contact with a completed Materials Transfer Agreement.

Data and code availability

The electron density and EM maps and their corresponding molecular models have been deposited to the Protein Data Bank (PDB) under accession codes PDB: 8CJW for the THOV-NP crystal structure and PDB: 8RYT for the THOV RNP cryo electron tomography structure. The cryo-EM map is deposited at the EMDB using accession code EMDB: EMD-19599. This paper does not report original code. Any additional information required to reanalyze the data reported in this paper is available from the lead contact upon request.

EXPERIMENTAL MODEL AND STUDY PARTICIPANT DETAILS

Protein overexpression was performed in *E. coli* BL21 (DE3) Rosetta strain (Novagen). For the polymerase reconstitution assay, THOV strain SiAr126 and HEK293T cells were used.

METHOD DETAILS

Protein expression and purification

Full-length THOV NP (Uniprot accession P89216), the indicated mutants, and a construct harboring an internal deletion of residues 188-196 ($NP^{\Delta 188-196}$) were expressed as N-terminal His_6-fusions from a pET28 plasmid followed by a PreScission™ cleavage site in the *E. coli* BL21 (DE3) Rosetta strain (Novagen). Bacterial cultures were grown in terrific broth at 37°C. At an OD_{600} > 0.4, cultures were cooled to 18°C, and protein expression was induced by adding 40 μM isopropyl-β-D-thiogalactopyranoside (IPTG). Following centrifugation, bacterial pellets were resuspended in ice-cold 50 mM HEPES (pH 7.5), 800 mM NaCl, 30 mM imidazole, 5 mM $MgCl_2$, 1 μM DNase I, 2.5 mM β-mercaptoethanol (β-ME), 500 μM Pefabloc SC (Roth), and lysed in a microfluidizer (Microfluidics). A soluble cell extract was prepared by ultracentrifugation at 35,000 g for 45 min at 4°C and, after filtration, applied to a Ni-NTA column (GE-Healthcare) equilibrated with 50 mM HEPES (pH 7.5), 400 mM NaCl, 30 mM imidazole, 5 mM $MgCl_2$, 2.5 mM β-ME. The column was extensively washed with 20 mM HEPES (pH 7.5), 800 mM NaCl, 5 mM $MgCl_2$, 50 mM imidazole, 2.5 mM β-ME, 1 mM ATP, 10 mM KCl, and afterward with 20 mM HEPES (pH 7.5), 400 mM NaCl, 5 mM $MgCl_2$, 50 mM imidazole, 2.5 mM β-ME. Following protein elution by 20 mM HEPES (pH 7.5), 400 mM NaCl, 300 mM imidazole, 5 mM $MgCl_2$, 2.5 mM β-ME, the protein was incubated overnight at 4°C in the presence of 250 μg GST-tagged PreScission protease to cleave the N-terminal His_6 tag. The cleaved protein was concentrated and applied to a Superdex 200 16/60 (G.E.) gel filtration column equilibrated with 20 mM HEPES (pH 7.5), 150 mM NaCl, 2 mM $MgCl_2$, 2 mM DTT. PreScission protease was removed using a GST column. THOV NP fractions were pooled, concentrated, and frozen in small aliquots.

Analytical gel filtration

The THOV NP mutants were analyzed using an Aekta Purifier (GE Healthcare) equipped with a Superdex 200 10/300 column. The running buffer contained 20 mM HEPES (pH 7.5), 150 mM NaCl, 2 mM $MgCl_2$. A flow rate of 0.5 mL/min was used. Chromatograms were recorded at a wavelength of 280 nm.

Analytical ultracentrifugation

The oligomeric state of the NPs was determined by AUC in gel filtration buffer (150 mM NaCl) using a Beckman Optima XL-I-type analytical ultracentrifuge equipped with ultraviolet absorbance optics. Samples were measured in an An-50 Ti rotor at a wavelength of 280 nm with a radial spacing of 0.003 cm. The protein was used in a concentration of 0.5 mg/mL. Sedimentation velocity experiments were carried out at 35,000 revolutions per minute (rpm) at 10°C, using two-channel cells with a 12 mm optical path length and a 400 μL sample volume. Sedimentation coefficient distributions were analyzed with the program Sedfit.[46] The protein partial-specific volume and the buffer physical constants were calculated from amino acid and buffer composition, respectively, using SEDNTERP.[47]

Right angle laser scattering (RALS)

A coupled RALS system and Refractive Index detector (Malvern) was connected in line to an analytical gel filtration column Superdex 200 10/300 to determine the absolute molecular masses of the applied protein. 20 mM HEPES pH 7.5, 150 mM NaCl, 2 mM MgCl2, and 2 mM DTT was used as running buffer with a flow rate of 0.5 mL/min. 50 μL of a 4 mg/mL THOV NP solution was applied. Data analysis was performed with the provided software (Omnisec).

Crystallization and data collection

Protein crystallization of native and selenomethionine (SeMet)-substituted THOV $NP^{\Delta 188\text{-}196}$ protein was performed at 10 mg/mL. The native crystals grew in 21% PEG 1500, 0.1 M spiroglycol pH 7.0, and the SeMet-crystals in 20% (w/v) PEG 3350, 200-300 mM NaCl after 1 week at 4°C using the sitting drop vapor diffusion method in 96-well plates and the hanging drop method in 24-well plates, respectively, using a protein:precipitant ratio of 1:1. The dataset for the native THOV $NP^{\Delta 188\text{-}196}$ crystals was recorded at 100 K and a wavelength of 0.91841 Å at beamline 14.1 at BESSY II, Berlin-Adlershof, using a Pilatus 6M detector.

A dataset of the SeMet-containing THOV $NP^{\Delta 188\text{-}196}$ crystals was collected at the DESY synchrotron radiation facility in Hamburg, Petra III (P11), equipped with a Pilatus 6M detector at the selenium peak wavelength of 0.97973 Å. All crystals were cryo-protected by addition of 20% ethylene glycol to the mother liquor before flash freezing into liquid nitrogen.

Atomic model building and refinement

The phases for the THOV $NP^{\Delta 188\text{-}196}$ structure were obtained using SAD. 9 out of 11 selenium atoms were found with SHELXD[48] using the anomalous signal of the peak data sets. Initial phases were calculated with SHELXE and HKL2MAP.[49] Initial model building was performed with Coot.[50] Selenomethionine positions were used to allocate the sequence. Molecular replacement with Phaser[51] was done with the native data using the initial build model. Refinement was done with Phenix[52] using TLS (Translational, libration, screw rotation displacement) refinement. 5% of the measured X-ray intensities were set aside from the refinement for cross-validation. The electrostatic surface potential and other figures were prepared with the PyMOL Molecular Graphics System, Version 2.5.2, Schrödinger. The conservation plot was calculated using the Consurf server[53] and visualized with Chimera.[54]

Grid preparation and image acquisition for cryo-ET

THOV RNPs were isolated from THOV particles collected from the supernatants of infected cells as described previously.[29] Purified virions were lysed using 0.5% NP-40, 1.0% Triton X-100 and 10 mg/ml lysolecithin and separated by centrifugation through a glycerol gradient at 135,000 relative centrifugal force (rcf) for 5 hours. To remove glycerol, 50 μl of the purified RNP fraction was diluted with 450 μl 50 mM Tris (pH 8.0), 5 mM $MgCl_2$, 100 mM KCl, 1.5 mM DTT and concentrated in a 50 kD Amicon centrifugation filter to a final volume of ~30 μl. The sample was kept on ice and applied to an R2/2 Cu 300-mesh holey carbon-coated grid (Quantifoil, Germany). Grids were plunged using a VitroBot Mark IV at 95% humidity and 4°C in the incubation chamber.

THOV-RNP data was acquired on thin carbon film. Data was recorded using a Titan Krios G3i electron microscope operating at 300 kV equipped with a K3 direct electron detector and a BioQuantum post-column energy filter in energy filtered zero-loss (slit width 20 eV) nano-probe super-resolution counting mode. The nominal magnification was set to 33,000 at a calibrated pixel size of 1.3 Å. Tomographic tilt series were collected using SerialEM 4.0 beta[55] using a dose-symmetric tilting scheme[56] with 3° increment, resulting in an angular coverage from -48° to +48° and a cumulative total electron dose of ~115.5 $e^- Å^{-2}$. The defocus values during acquisition ranged from -3 to -7 μm. Dose-fractionated movies were collected at each tilt consisting of 10 fractions.

THOV-RNP tomogram reconstruction and subtomogram averaging

44 tilt series of THOV-RNP were processed in TomoBEAR[57] starting from raw super resolution fractions (Å/pix = 1.3). Fractions were imported and sorted, followed by global motion correction with 2x Fourier cropping with MotionCor2.[58] Stacks were assembled and subjected to global alignment with AreTomo[59] with a specified tilt axis value of 84° without refinement. Aligned tilt series were visually inspected, and misaligned tilt series were excluded, leaving 33 tilt series for the downstream processing. CTF was estimated and

phase flipping on tilt images was performed with GCTF,[60] followed by tomogram reconstruction from the CTF-corrected aligned tilt series. GPU-accelerated Dynamo template matching[61] was performed with a 360° search range and a 5° angular search step size using a featureless cylinder as a reference. At this point, the TomoBEAR workflow was finished and the remaining steps were performed interactively. Motion-corrected untilted images were exported to RELION4[62] and helices were manually traced. Particles representing tube segments were extracted, binned 4x and subjected to 2 rounds of 2D classification. XY coordinates of particles from the selected classes showing clear helical features were used to mask cross-correlation volumes during subtomogram extraction to avoid empty or contaminated regions. The extracted 16,101 subtomograms were directly imported into RELION4 tomo[63] and subjected to one round of 3D classification in bin4 into 8 classes with global angular search and helical reconstruction mode, but without applying any symmetry. 5,578 particles from two selected classes were auto-refined, and the resulting map showed a clear presence of helical symmetry, which was applied to all successive runs. The helical symmetry parameters were estimated to be: box size = 670 Å, sphere diameter = 400 Å, outer helix diameter = 170 Å, number of asymmetric units = 10, central Z fraction = 0.4, twist = 55.5°, rise = 24.6 Å. After auto-refinement in bin2, subtomograms were re-extracted with 2x smaller box size (340 Å) and subjected to another round of auto-refinement and 3D classification without alignment into 4 classes. 3,228 particles from the best class were selected and auto-refined, followed by one round of tilt series alignment refinement and per-particle motion fitting ("TomoFrameAlignment"). Although the subtomograms were extracted on non-overlapping segments, some particles converged on the same positions after all alignment rounds; therefore, particles closer than 1 helical rise were excluded, leaving 3,128 particles. The final round of auto-refinement with a 500 Å box size produced a map at 17.8 Å resolution. A cylindrical mask with soft-edges covering 1 central helix turn was used at all alignment rounds and for resolution estimation with FSC. Model fitting was performed by manual adjustment of three neighbored molecules from an AlphaFold predicted hexameric ring structure into the map using Coot and the Chimera 'Fit in Map' tool.[50] Copies of the fitted molecules were used to fill one round of the double-helical RNP. Afterwards real space rigid body refinement cycles with Phenix were performed.[52] Figures were prepared with the PyMOL Molecular Graphics System, Version 2.5.2, Schrödinger.

Validation of the handedness of STA structures

A small data set of 9 tilt series of purified ribosome large subunit (LSU) was recorded on the same microscope in the same month and subjected to the same processing pipeline in TomoBEAR as for THOV RNP starting from raw super resolution fractions (Å/pix = 2.243). Fractions were imported and sorted, followed by global motion correction with 2x Fourier cropping with MotionCor2. Stacks were assembled and subjected to global alignment with AreTomo with a specified tilt axis value of 84° without refinement. CTF was estimated and phase flipping on tilt images was performed with GCTF, followed by tomogram reconstruction from the CTF-corrected aligned tilt series. GPU-accelerated Dynamo template matching was performed with a 360° search range and a 5° search step with a featureless blob of LSU size as a reference. At this point, the TomoBEAR workflow was finished and the remaining steps were performed interactively. 30,298 particles were imported into RELION4 TOMO and subjected to 3 rounds of 3D classification at bin2 into 8 classes with global angular search and spherical mask. The final selection of 5,451 particles was subjected to auto-refinements at bin2 and bin1, followed by TomoFrameAlignment (with motion), CTF refinement (without high-order aberrations) and a final auto-refine that produced a map at 9 Å resolution (Nyquist frequency). The LSU model (PDB: 6LSS) was placed and fitted into the map with Chimera.[54]

RNA-binding studies

Nucleotide dissociation constants of THOV NP to single-stranded RNA of varying length (pU14 - pU24) were determined at 8°C on an VP-Isothermal titration calorimetry (VP-iTC) system (MicroCal™, GE Healthcare, Freiburg). 150 μM single-stranded RNA in ITC Buffer (50 mM HEPES (pH 7.5), 150 mM NaCl, 5 mM $MgCl_2$, 5 mM KCl) was titrated in 8 μL steps into a reaction chamber containing 10 μM of WT THOV NP (or the $NP^{\Delta 188\text{-}196}$ variant) in the same buffer. Titration of single-stranded pU24 to THOV NP RNA-binding groove mutants or to WT THOV was performed at the iTC_{200}-Isothermal Titration Calorimetry (iTC_{200}) system (MicroCal™, GE Healthcare, Freiburg) due to less available material. 300 μM single-stranded pU24 RNA in ITC Buffer (50 mM HEPES (pH 7.5), 150 mM NaCl, 5 mM $MgCl_2$, 5 mM KCl) was titrated in 2 μL steps into a reaction chamber containing 20 μM of THOV NP (or the indicated mutants) in the same buffer. The resulting heat change upon injection was integrated over a time range of 240 sec, and the obtained values were fitted to a standard single-site binding model using Origin®.

Polymerase reconstitution assay

To assay the polymerase activity of THOV strain SiAr126 (ref.[64]), 293T cells were seeded into 12-well plates and transfected with 10 ng pCAGGS expression plasmids[65] for the viral polymerase subunits PB2, PB1, and PA as well as 50 ng NP-encoding plasmid and 50 ng of a reporter plasmid encoding *firefly* luciferase in negative-sense orientation flanked by 5'- and 3'-UTRs from viral segment 5 (pHH21-vNP-FFLuc for THOV[66]). 10 ng pRL-SV40, from which *Renilla* luciferase is constitutively expressed, was added to normalize transfection efficiency. Expression of the *firefly* luciferase reporter gene indicates transcriptional activity of the reconstituted polymerase complex. Each experiment contained technical duplicates and all experiments were performed three times. Statistical analysis was performed using the GraphPad Prism 6 software. For expression control, Western blots with specific antibodies against Flag- or HA-tag and β-actin (Sigma) were performed.

Please cite this article in press as: Dick et al., Structural characterization of Thogoto Virus nucleoprotein provides insights into viral RNA encapsidation and RNP assembly, Structure (2024), https://doi.org/10.1016/j.str.2024.04.016

Immunoblot analysis

293T cells were lysed in 50 mM Tris (pH 8.0), 150 mM NaCl, 1 mM EDTA, 0.5% Nonidet P-40 Alternative (Calbiochem) and incubated with anti-Flag-M2 affinity gel (Sigma) for 2 h at 4°C. The washed precipitates and whole-cell lysates to control protein expression were subjected to standard Western Blot analysis using antibodies against THOV NP[67] and β-actin (Sigma).

QUANTIFICATION AND STATISTICAL ANALYSIS

X-ray crystallography data collection and refinement statistics are shown in Table S2. Cryo-EM data collection, refinement and validation statistics are summarized in Table S4.